UNIVERSITÀ DI TRENTO | Dipartimento di Fisica

NANOSCIENCE LABORATORY

HIGHLIGHTS 2019

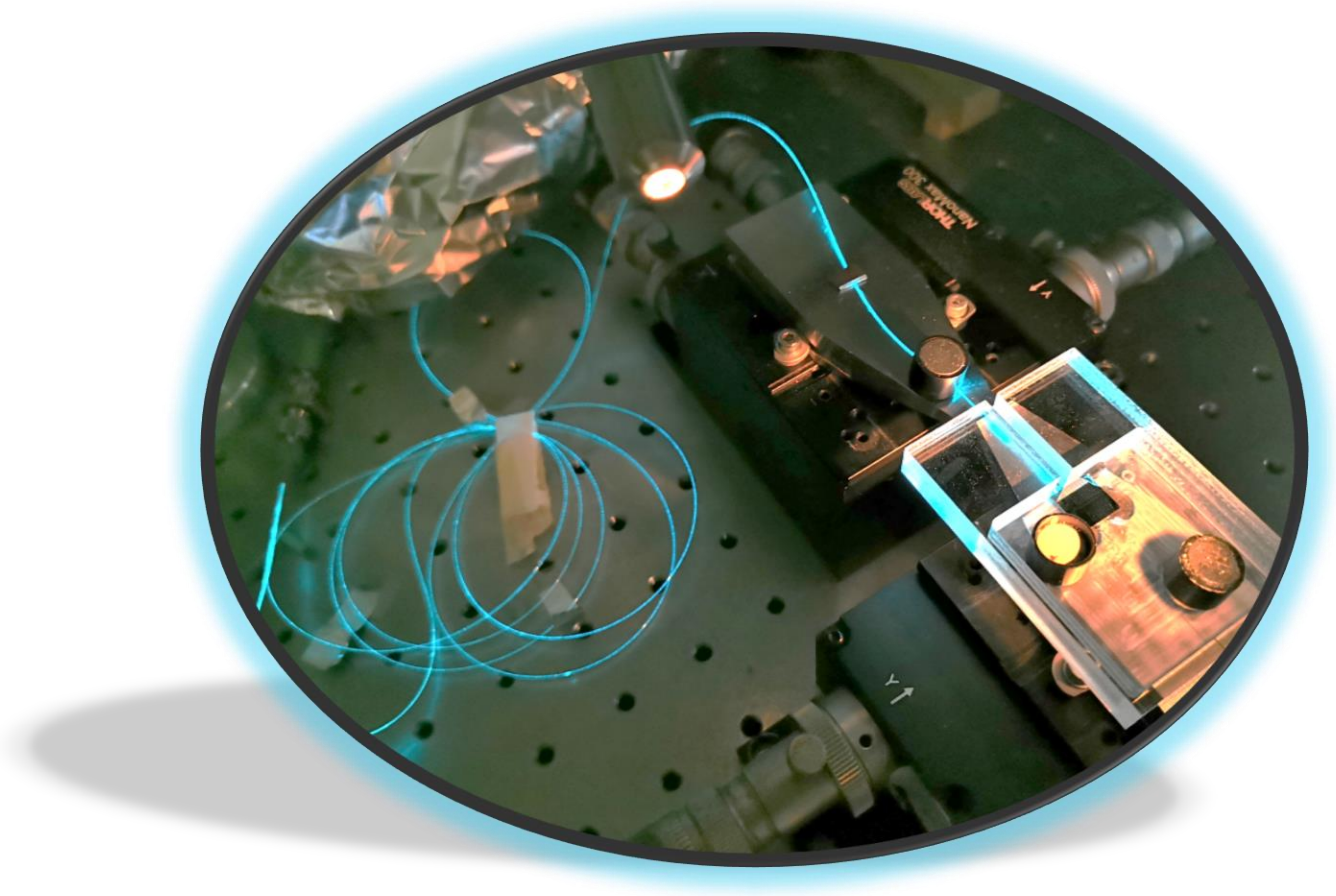

Image on the front cover:
The set-up to measure a photonic chip in the visible
Photo by C. Zaccaria

NANOSCIENCE LABORATORY

MEMBERS (2019)

Faculty staff
Lorenzo Pavesi (full professor, head)
Marina Scarpa (full professor)
Zeno Gaburro (associate professor)
Paolo Bettotti (associate professor)
Enver Sangineto (researcher)
Mattia Mancinelli (researcher)
Beatrice Vignoli (researcher)
Stefano Azzini (assistant professor)

Technical staff
Enrico Moser
Giorgio Fontana (EP7 level)
Elvira D'Amato

Post-docs
Stefano Signorini

Administrative staff
Chiara Rindone

Doctoral students
Claudio Castellan (left March 2019)
Chiara Piotto (left April 2019)
Sara Piccione
Stefano Biasi
Chiara Vecchi
Clara Zaccaria
Davide Bazzanella
Nicolò Leone
Riccardo Franchi
Dhouha Jemmelli
Giovanni Donati

Master students
Damiano Lodi (left March 2019)
Andrea Volpini (left July 219)
Mattia Finazzer (left October 2019)

SCIENTIFIC MISSION

Introduction to the Nanoscience Laboratory

The Nanoscience Laboratory (NL) is one of the scientific groups of the Department of Physics, University of Trento. Its main areas of research are neuromorphic photonics, integrated quantum photonics, linear and nonlinear silicon photonics and nanobiotechnologies. The mission of NL is to generate new knowledge, to develop understanding and to spin-off applications from physical phenomena associated with photons and their interactions with matter, particularly when it is nanostructured. Specifically, NL aims at understanding the optical properties of ligthwave systems such as optical waveguides, microresonators and complex dielectric systems. NL covers the whole value chain from fundamental phenomena to device applications, where the photonic platform is compatible with the main driving silicon microelectronic technologies. However, silicon is not the only material studied. Other fields of interest concern the use of cellulose to tailor the properties of nanostructure atom-by-atom or the use of perovskites to investigate their new properties.
NL research group consists of more than 20 people with different scientific backgrounds. Researchers from physics, physiology, bio-chemistry, materials science and electrical engineering are gathered to form a group of interdisciplinary nature. It is worth mentioning that NL collaborates closely with the Center of Materials and Microsystems, Fondazione Bruno Kessler (FBK). This collaboration spans over the last thirty years and covers various topics such as fabrication, testing and application of biomaterials and silicon based devices. Both participate in many common projects. The current ones are: projects LESSO, NEMO, QRANGE and Q@TN. A new strategic collaboration is ongoing with the Trento units of CNR-INO, specifically dedicated to implement quantum optics in integrated silicon chip.
Moreover, with the support of FBK and CNR and every odd year, NL organizes a winter school on optoelectronics and photonics. The 10th edition was organized on "Nonlinear Photonics" (20-26 January, 2019) and the 11th edition will be on "Neuromorphic Photonics" in early 2021. Furthermore, the members of NL are often invited to participate in the organizing committees of international conferences or workshops.
The research activities of NL are mainly supported by the local government (PAT), by the European Commission, by the Italian Ministry of Education, University and Research (MIUR) and by companies. During the period covered by these Highlights, NL has been and is involved in the following projects: PRIN-MIUR NEMO "Nonlinear dynamics of optical frequency combs"; PRIN-MIUR PELM "Photonics Extreme Learning Machine: from neuromorphic computing to universal optical interpolant, strain gauge sensor and cancer morphodynamic monitor"; PRIN-MIUR PANACEA "A technology PlAtform for the sustainable recovery and advanced use of NAnostructured CEllulose from Agri-food residues"; ERC-2017-ADG-788793 BACKUP: "Unveiling the

relationship between brain connectivity and function by integrated photonics"; H2020-FETFLAG-2018-03 QRANGE: "Quantum Random Number Generators: cheaper, faster and more secure"; Q@TN project "Quantum Science and Technology in Trento"; India-Trento Program for Advanced Research - ITPAR: "A cheap, light, compact source for QKD based on intraparticle entanglement in an integrated photonic circuit"; ASI - LESSO: "Laser etero-integrato a stato solido per trappole ottiche"; NANOFARM (Legge Provinciale 13 dicembre, 1999 n. 6).

Silicon Nanophotonics

Silicon photonics is the technology where photonic devices are produced by standard microelectronic processes using the same paradigm of electronics: integration of a large number of devices to yield a high circuit complexity, which allows for high performances and low costs. Here, the truth is to develop photonic devices that can be easily integrated to improve the single device performance and to allow high volume production.

In the next year we will mostly concentrate on two alternative approaches where photonics is used to compute. On one side we will develop new scheme to implement artificial intelligent in a photonic silicon chip by using brain-inspired or neuromorphic computing schemes. On the other side, we will use silicon photonics to provide a suitable platform for quantum computing and quantum simulations. In both approaches one fundamental device is the silicon microresonator where whispering gallery modes induce nonlinearities which can be exploited to generate new quantum states of light or to realize recurrent neural network. In addition, we use micro-disks or micro-rings to study new physics (chirality, frequency comb generation, entangled photon generation). The microresonators are coupled directly with narrow mode SOI (Silicon-on-Insulator) waveguides. Also, multimode waveguides are used for nonlinear frequency conversion or generation.

To develop silicon photonics, one further add-on is making silicon to do something that it is not able to do in its standard (bulk) form. Low dimensional silicon, where small silicon nanocrystals or nanoclusters (Si-nc) are developed, is one way to compel silicon to act as an active optical material. Alternatively, we use the built-in or p-i-n induced electric fields to tune the non-linear optical properties of silicon waveguides for the development of new MIR sources (parametric generation via second order effects or frequency comb generation). Nonlinear optics is finally used to generate pairs of entangled photons, which in turn feed quantum interferometers or integrated quantum photonic circuits.

Lastly, hybrid chips are developed to interface living neurons with photonic waveguides in the search for artificial intelligence. Here, the signal transduction is achieved by using photo-sensitive proteins.

Advanced nanomaterials for energy, environment and life.

In this research activity, we learn from nature how to use molecules or biological nanostructures to build materials with specific features. The focus is on understanding the properties of colloids of biological origin, the dynamics at the bio-interfaces, the strength and stability of natural structures. The final goal is to transfer the acquired knowledge on innovation by developing sustainable and smart materials and processes.

Experimental facilities

The NL facilities allow for detailed experimental studies in nanoscience, photonics and biotechnologies. Since the effective collaboration with FBK most material processing and device productions are performed within their premises. For photonics, we have facilities to cover the light spectrum from the THz to UV ranges with whatever time resolution is needed. Laser sources comprehends: Ti-sapphire fs-ps laser (1 W average over 1000-700 nm, 2 ps or 70 fs pulses, 82 MHz repetition rate) interfaced with a second harmonic generator and pulse picker; TOPAS pumped with an amplified Ti:Sa laser which covers the 1-2.6 μm range with 35 fs, 10 kHz, 3 mJ; 2W tunable CW Cr:ZnSe/S fiber-bulk hybrid laser to cover the 2-3 μm range; four tunable CW lasers (850-870 nm, 1200 - 1700 nm and 1500 - 1600nm) fiber pig-tailed; high power fiber-laser at 1550 nm (1-100 MHz, 50 ps); 4W EDFA and 2W semiconductors amplifiers, a supercontinuum light source (410-2400 nm, 1W), several pig-tailed diode lasers, ASE source at 1550 nm and a broad band SLD at 800 nm; three high-power true-CW DPSS single-line laser operating at 532, 473 and 355 nm. Detectors comprehend: visible and infrared photomultipliers and CCDs, a visible streak camera with ps resolution, 4K cooled bolometers which cover THz region, avalanche photodiodes for vis and IR ranges plus many single photon detectors in the visible and IR. Two home-made MIR single photon-counters. To perform spectral analysis several set-ups are available: FTIR and dispersive spectrophotometers, a micro-Raman setup, a micro-FTIR and a UV-vis-IR spectrophotometer (shared with other laboratories), UV-Vis and fluorescence spectrophotometer dedicated to biochemical experiments. Eight set-ups are dedicated to the characterization of waveguides equipped with nanopositioning systems and polarization controllers, each specified on a given function: visible, visible broad range, quantum, passive infrared, high speed infrared, non-linear infrared, non-linear MIR and on wafer. A set-up is dedicated to high speed measurements, with 80 Gbps capability where a 60 GHz arbitrary waveform generator, electro-optical modulators, coherent detectors and a four channels, 20 GHz oscilloscope. Other devices are: - a solar simulator for cells up to 5 inches in size; - two nanoprobe stations (AFM and

SNOM) - two semiconductor probe stations (4 and 8 inches) and different electrical characterization systems (I-V, Z-Ω, EL-I, etc.). Four VIS to NIR optical spectrum analyzers are available. A probe station is interfaced by a fibres bundle with a spectrometer equipped with nitrogen cooled visible and IR CCDs. An electrochemical laboratory with various chemical hoods, galvanostats and volt-ameters is available for sample processing. For optical, electrical and molecular dynamics simulations, the laboratory uses free and commercial software and has a work-station with 4 GPU. Two laboratories are also available, one dedicated to chemical synthesis and the other to the preparation of biological samples. Two other laboratories with biological hoods, incubators and confocal microscopes are dedicated to biological experiments. In one, a confocal microscope with an insert for electrophysiology (MEA) and optogenetics measurement equipped with a "spinning disk" system for fast acquisitions and a super-resolution system.

2019 Publications

- Massimo Borghi, Alessandro Trenti, Lorenzo Pavesi "Four Wave Mixing control in a photonic molecule made by silicon microrings resonators", Scientific Reports 9:408 (2019).
- Stefano Biasi, Fernando Ramiro-Manzano, Fabio Turri, Pierre-Elie Larrè, Mher Ghulinyan, Iacopo Carusotto, Lorenzo Pavesi "Reconfigurable and Non-Hermitian mode coupling in a micro-disk resonator due to stochastic surface roughness scattering" IEEE Photonics Journal 11, 6101114 (2019).
- Francesco Testa, Stefano Tondini, Fabrizio Gambini, Philippe Velha, Alberto Bianchi, Christophe Kopp, Michael Hofbauer, Costanza L. Manganelli, Nikola Zecevic, Stefano Faralli, Gabriel Pares, Reinhard Enne, Aina Serrano, Bernhard Goll, Giorgio Fontana, Astghik Chalyan, Jong-Moo Lee, Paolo Pintus, Guido Chiaretti, Horst Zimmermann, Lorenzo Pavesi, Claudio J. Oton, Stefano Stracca, "Integrated Reconfigurable Silicon Photonics Switch Matrix in IRIS Project: Technological Achievements and Experimental Results", Journal of Lightwave Technology 37, 345-355 (2019).
- Tatevik Chalyan, Cristina Potrich, Erik Schreuder, Floris Falke, Cecilia Pederzolli, Rene Heideman, Lorenzo Pavesi, "AFM1 detection in milk by Fab' functionalized Si3N4 Asymmetric Mach-Zehnder Interferometric biosensors" Toxins 11, 409 (2019).
- Claudio Castellan, Alessandro Trenti, Chiara Vecchi, Alessandro Marchesini, Mattia Mancinelli, Mher Ghulinyan, Georg Pucker, and Lorenzo Pavesi "On the origin of second harmonic generation in silicon waveguides with silicon nitride cladding" Scientific Report 9, 1088 (2019).
- S. Biasi, P. Guilleme, A. Volpini, G. Fontana, L. Pavesi "Time response of a microring resonator to a rectangular pulse in different coupling regimes" IEEE Journal of Lightwave Technology 37, 5091-5099 (2019).
- Stefano Tondini, Claudio Castellan, Manuel Medina, Lorenzo Pavesi "Automatic initialization methods for photonic components on a silicon-based optical switch" Applied Sciences 9, 1843 (2019).
- L. Lunelli, F. Caradonna, C. Potrich, C. Piotto, P. Bettotti, L. Vanzetti, C. Pederzolli, G. Guella "A new silanizing agent tailored to surface bio-functionalization", Colloids and Surfaces B: Biointerfaces, 181, 166 (2019).
- Claudio Castellan, Riccardo Franchi, Stefano Biasi, Martino Bernard, Mher Ghulinyan, Lorenzo Pavesi "Field-induced nonlinearities in silicon waveguides embedded in lateral p-n junctions Manuscript", Frontiers in Physics, section Optics and Photonics 7, 104 (2019).
- Stefano Signorini, Matteo Finazzer, Martino Bernard, Mher Ghulinyan, Georg Pucker, Lorenzo Pavesi "Silicon photonics chip for inter-modal Four Wave Mixing on a broad wavelength Range" Frontiers in Physics, section Optics and Photonics 7, 128 (2019).
- Stephane Lathuilière, Enver Sangineto, Aliaksandr Sirohin, Nicu Sebe "Attention-based Fusion for Multi-Source Human Image Generation" (2019).

- Aliaksandr Siarohin, Stéphane Lathuilière, Enver Sangineto, Nicu Sebe "Appearance and Pose-Conditioned Human Image Generation using Deformable GANs" on IEEE Transaction on Pattern Analysis and Machine Intelligence, (2019).
- Subhankar Roy, Aliaksandr Siarohin, Enver Sangineto, Samuel Rota Bulò, Nicu Sebe, Elisa Ricci "Unsupervised Domain Adaptation using Feature-Whitening and Consensus Loss" Computer Vision and Pattern Recognition (CVPR) (2019).
- S. Meschini, E. Pellegrini, C. A. Maestri, M. Condello, P. Bettotti, G. Condello, M. Scarpa "In vitro toxicity assessment of hydrogel patches obtained by cation-induced cross-linking of rod-like cellulose nanocrystals", Journal of Biomedical Materials Research Part B: Applied Biomaterials (2019).
- C. Piotto and P. Bettotti "Surfactant mediated clofazimine release from nanocellulose-hydroge", Cellulose 26, 4579 (2019).
- M. Biesuz, P. Bettotti, S. Signorini, M. Bortolotti, R. Campostrini, M. Bahri, O. Ersen, G. Speranza, A. Lale, S. Bernard, G. D. Soraru "First synthesis of silicon nanocrystals in amorphous silicon nitride from a preceramic polymer" Nanotechnology 30, 255601 (2019).
- Aliaksandr Siarohin, Enver Sangineto, Nicu Sebe "Whitening and Coloring batch transform for GANs, ICLR conference (2019).

2019 PhD Thesis:

- Claudio Castellan "Second order nonlinearities in silicon photonics" (22nd March 2019)
- Chiara Piotto "Nanostructured materials for hydrophobic drug delivery" (11th April 2019)
- Stefano Signorini "Intermodal four wave mixing for heralded single photon sources in silicon" (10th of July 2019)

1. Control of the photo-luminescence of a 2D semiconductor by a plasmonic antenna (Stefano Azzini)

Two-dimensional semiconductors (Transition Metal Dichalcogenides, TMDs) are quasi-2D monolayers (MLs), comprising three planes of covalently bound atoms (Fig. 1a): one plane of transition metal atoms (M, either Molybdenum or Tungsten) coordinated with two planes of chalcogen atoms (X, either Sulphur, Selenium or Tellurium), for a total thickness of less than 1 nm. The quantum confinement of these sub-nanometre structures leads, on one side, to direct optical bandgap and strong Coulomb interactions for which Wannier-type tightly-bound excitons (binding energy in the range 0.3-1 eV) dominate the optical spectra, with absorption in excess of 10% and intense light emission, both at the ML level. On the other side, the broken inversion symmetry within the unit cell and the large spin-orbit coupling are responsible for a locking mechanism between the spin of the electrons and the valley they occupy in momentum space. In particular, electrons in opposite valleys have opposite spins and their transitions between valence and conduction bands are governed by opposite selection rules as to the conservation of the electron orbital angular momentum. This translates into a selective addressability of excitons in opposite valleys by means of light with opposite helicity (circular polarization), namely the possibility to optically manipulate the so-called valley pseudo-spin degree of freedom of excitons, which leads to the new field of research of valleytronics.

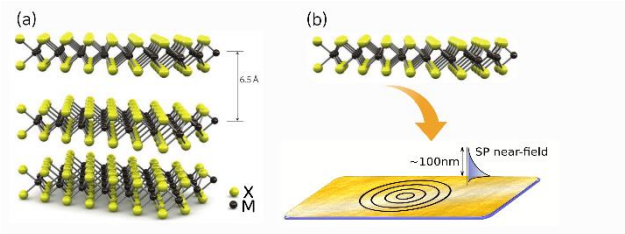

Figure 1. (a) *Three-dimensional representation of a typical MX_2 structure: ~6.5 Å single layers can be isolated via scotch tape-based mechanical exfoliation (chalcogen atoms X in yellow, transition metal atoms M in black);* ***(b)*** *sketch not to scale of a TMD ML transferred into the near-field of a plasmonic bullseye antenna.*

Plasmonic antennas are an example of the optical counterpart of what traditional macroscopic antennas represent for, e.g., a radio-frequency field. A radiation-emitting object can experience an enhancement of its emission features by means of the interaction with a suitable antenna. This last is able to mediate the interaction both in absorption and emission and, therefore, influences the brightness, directionality or polarization of the radiation-emitting object. In 2D semiconductors, the emitting dipoles are the valley excitons whose radiative recombination results in the emission of photons having a polarization which carries information about the dynamics of the excitons themselves. For example, valley polarization is the efficiency with which these valley excitons store and return the information carried by the spin of the exciting photons. However, because of inter-valley scattering processes, this is typically vanished at room-temperature (RT) in a bare 2D semiconductor. Following the observations of robust RT valley polarization and of coherence in a TMD coupled to a plasmonic spin-orbit array or to a graphene ML, the idea behind our experiments is: given that a plasmonic antenna can enhance the decay rate and dominate the polarization of a coupled emitter, what does it happen to the photo-luminescence (PL) of a 2D semiconductor ML lying in such a surface plasmon (SP) near-field (Fig. 1b)?

We carried out RT polarimetry experiments of the PL of a WS_2 ML transferred on top of a plasmonic antenna (Fig. 2a) resonant with the A-exciton energy of WS_2 (at 2 eV). Measuring the Mueller matrices of the light emitted from such a 2D semiconductor-antenna hybrid, we have observed both the enhancement of PL directionality (Fig. 2b) and a high-degree of PL polarization (Fig. 2c), a proof of the extremely good antenna-emitter coupling, which points towards a SP-induced valley polarization and coherence of the atomically thin semiconductor at RT. Moreover, we stress that Mueller polarimetry is the proper tool for a correct quantitative evaluation of the polarization properties of 2D semiconductors emission on top of optical antennas and metamaterials structures.

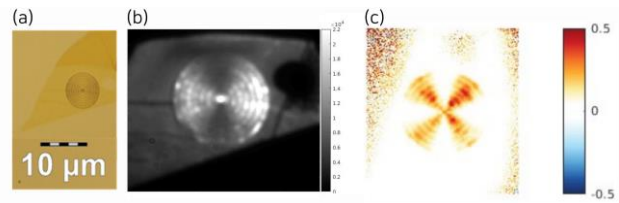

Figure 2. (a) *Optical micrograph of an exfoliated WS_2 ML transferred on top of a bullseye plasmonic antenna;* ***(b)*** *horizontally polarized PL emission from the sample shown in (a);* ***(c)*** *m_{02} Mueller matrix element (maintaining of linear polarization, i.e. measurement of valley coherence) of the PL microscopy polarimetry imaging performed on the sample in (a).*

These experiments have been carried out at the Laboratoire des Nanostructures led by Prof. Thomas W. Ebbesen at the Institut de Science et Ingégnerie Supramoléculaires (ISIS) of the University of Strasbourg & CNRS, under the supervision of Dr. Cyriaque Genet and in collaboration with the team of Prof. Stéphane Berciaud, also based in Strasbourg. In close collaboration with these research groups, these subjects continue to be further developed

2. Design of an external cavity semiconductor for intra-cavity beam combing (Sara Piccione)

Semiconductor or diode lasers are playing an increasingly important role in optics, thanks to several advantages with respects to other type of laser. Nevertheless, the maximum

power extracted from a single laser diode chip is typically around some tens of watt. Several processes contribute to this limitation and among these there are Catastrophic Optical Damage (COD), nonlinear phenomena and thermo-optical distortion caused by the injection current. Thus, the increase of the diode laser power is one of the primary goals to promote a wider application of diode lasers in industry. Nowadays, the most accomplished technique for power scaling relies on the combination of laser beams from different emitters.

Incoherent spatial beam combining consists of placing several emitters next to each other. The total power is increased at expense of the source brightness. In wavelength beam combining, sources emitting at different wavelength are combined through a diffractive optical element. The source radiance scales up with the number of emitters.

On the contrary, coherent beam combining relies on optical interference. All the elements must have a proper phase relation in order to guarantee the conditions for constructive interference. Depending on the application a particular architecture, or a combination of different approaches (incoherent and coherent), can be used.

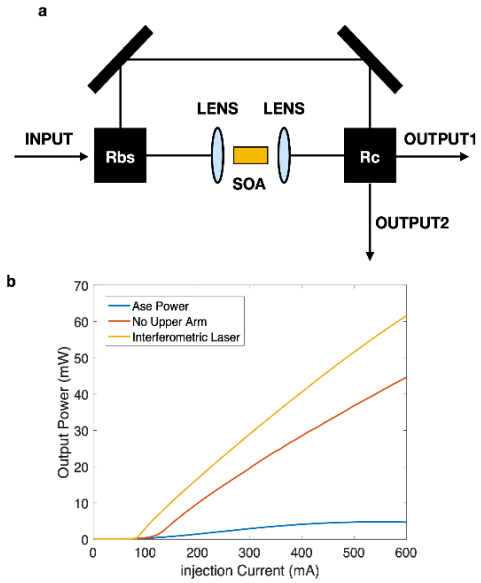

Figure 3. (*a*) *Scheme of the interferometric semiconductor amplifier.* ***(b)*** *Experimental results of the interferometric laser (yellow line). The red curve indicates the laser output power when the upper arm of the interferometer does not contribute. The comparison with the yellow curve clearly shows the power increase due to the constructive interference.*

We propose an innovative approach to scale up the diode laser power, which encompass a cascade of sequential interferometric optical amplifier (ISA) shown if fig. 3a, implemented in a common external resonant cavity. The overall system can be viewed as a unique Extended-Cavity semiconductor Laser, where the optical amplifier (SOA) is replaced by the ISA cascade. An ISA is realized by placing the SOA into one arm of an interferometer. The use of the combination of beam splitters and beam combiners allows the implementation of a sequence of SOA, otherwise not possible because of the gain saturation. The overall laser output power increases with the number of gain chips composing the whole device. The choice of each element realizing the cavity, including the length of each path, is crucial for the correct behavior of the laser.

A numerical model, based on the Rayleigh-Sommerfeld diffraction integral, to study the field propagation into the cavity was elaborated. The optimum configuration was found optimizing both the laser output power and the beam profile. To prove the validity of the model we first tested the ECL laser with a single ISA stage. By measuring the output power as a function of the injected current, a clear threshold behavior can be identified. Furthermore, the contribution of the interferometric arm (the yellow solid curve in fig.3b) is clearly visible. The two stages interferometric laser is currently under testing.

This work was supported by Adige spa of the BLM group.

3. Cellulose-based Nanomaterials: Structure and Properties (Paolo Bettotti, Marina Scarpa)

Cellulose nanocrystals are the rigid fundamental blocks composing plant cell walls. They are isolated from the macroscopic cellulosic fibers by removing the amorphous domains and they show peculiar chemical-physical characteristics.

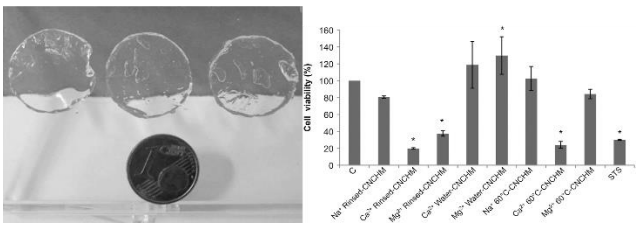

Fig. 4 *Nanocellulose gel patches; (right) Cell viability measured by washing the sample with different protocols. Untreated cells were used as control, first column.*

Cellulose nanocrystals are rigid sticks few hundreds nm long and with a cross section of about 10-20 nm^2. Their surface chemistry is flexible and, upon proper surface functionalization, large amount of surface charge can be imparted onto specific crystalline planes. Thus, the electrostatic interactions between the charge bearing groups and the water environment in which they are dissolved permit to tune the material properties and to realize materials spanning either liquid, gel as well as solid state.

We investigate the use of each of these phases to realize functional materials with ad-hoc characteristics for a broad range of applications (from mechanical actuators to film

with gas barrier property up to biomedical uses such as hydrogel for cell cultures and drug delivery).
Currently, with the support of a national research project (https://sites.google.com/unitn.it/panacea/home), we are exploring the possibility to recover cellulose-based high added value products from agri-food residues.

4. Astrocytes and memory engram (Beatrice Vignoli)

Understanding the cellular mechanisms of learning and memory remains one of the central goals of neuroscience. Memories are believed to be stored as permanent changes in the brain ("engram") involving a reinforcement of synaptic connections among specific neurons. The existence of an engram ensemble of cells was first demonstrated by using a learning- induced strategy for the expression of a channelrhodopsin in cell activated by the learning, that when they are stimulated by artificial light allow memory retrieval. It is widely believed that the principal mechanisms by which pre-existing synapses can strengthen their connections are long-term potentiation (LTP) and long-term depression (LTD).
While astrocytes have been considered for a long time to only perform supportive function for neurons in the central nervous system, they have recently described as an integral part of the synapse. In fact, astrocytes can modulate synapses homeostasis by restoring ion gradients, removing and releasing factors. Considering that a single astrocyte can cover thousands of synapses in the rodent brain (and even more in human) and that different astrocytes can communicate each other via gap junctions allowing the spreading of information along glial syncytium, these cells appear as ideal candidate for orchestrate the synaptic engram. However, only little is known about the dynamics of signaling adapting glial physiology to synaptic demand in memory circuits.
We are now investigating the role of astrocytes in functional and molecular aspects that may contribute to memory formation and consolidation. We found that cortical astrocytes, provide proBDNF clearing and re-release following long-term potentiation (LTP)-inducing neuronal activity. This mechanism of recycling represents a new way of gliotransmission essential for maintenance of long- term potentiation (LTP) and for object recognition memory consolidation. Thus, astrocytes could provide local support in the strength of neuronal connections playing a crucial role in learning and memory mechanisms.

5. Neuronal excitation through optogenetics (Beatrice Vignoli, Clara Zaccaria)

The term memory is referred to the storage of information in the brain. It is now widely believed that information could be stored in the brain as physical persistent modification of a subset of neurons which form a so-called engram. These permanent changes involve reinforcement of synaptic connections among specific neurons that are activated during the encoding of a memory trace.
The recent development of optogenetics techniques allowed the identification of single memory traces in the brain by inducing the selected expression of light- sensitive cell membranes channels (Channel rhodopsin) in a group of cells composing the engram during memory formation; activation of these selected cells by light induces memory re-activation.

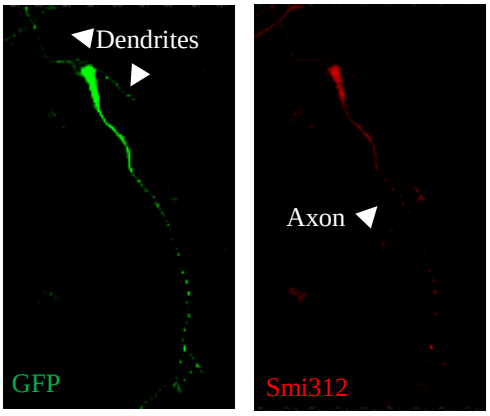

Figure 5. *Cultured cortical neuron expressing GFP (green) stained for specific axonal marker SMI 312 (red).*

Neuronal cultures attachment, growth and development of cells are strictly dependent on attachment factors and extracellular matrix application. Using poly-L-Lysine coating, we obtained neurons showing the typical morphological developmental steps described for neuronal culture in the literature. To further evaluate steps of maturation of neuronal culture we performed immunocytochemistry for different markers for axon (SMI312, $p75^{NTR}$), dendrites (MAP2) and growth cone Phalloidine, Tubulin). Spinning disk confocal images show that cultured neurons on glass coverslip provides stereotypical morphological features of *in vitro* neuronal differentiation, since they display a SMI312 positive axon (Fig. 5) and MAP2 positive dendrites.

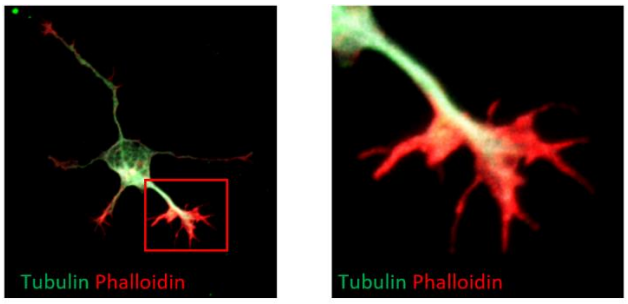

Figure 6. *(left) a cultured cortical neuron at day-in-vitro DIV3 stained for tubulin (green) and phalloidin (red). (right) 3-fold magnification of a growth cone.*

Moreover, growth cone shows appropriate cytoscheleton organization visualized by phalloidin staining in the outer part of the cone and tubulin labeling the inner part of extending processes (Fig. 6).

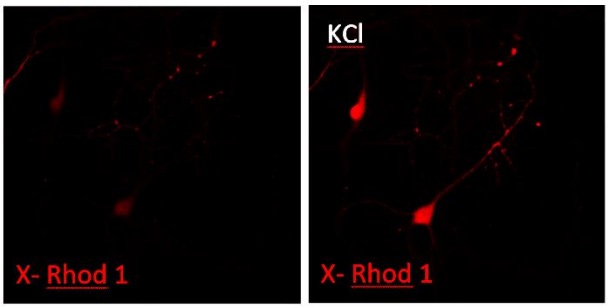

Figure 7. *(left) cultured cortical neurons labelled with calcium indicator X-Rhod 1. (right) X-Rhod 1 signal in the same neurons following KCl stimulation.*

To evaluate activity of the neuronal network we performed calcium imaging experiments using labeled calcium indicator (Fluo-4 and x-Rhod 1 AM ester forms) on culture at different ages. We stimulated neurons by adding to the bath culture KCl (40 mM) and we simultaneously record Ca2+ fluorescence using confocal spinning disk microscopy. We were able to observe an increase in fluorescence level of the indicator in different compartments of the cells such as cell body and fine processes (Fig. 7) proving that neurons are functionally active.

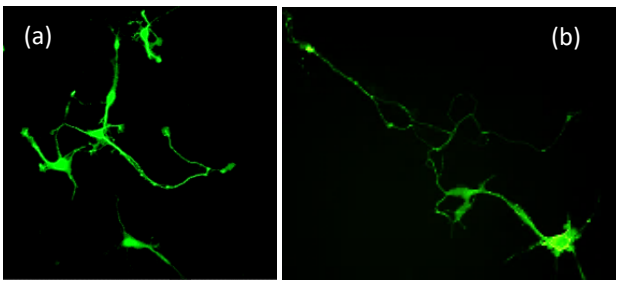

Figure 8. (a) *Cultured cortical neurons transfected with GFP. Cell bodies are dispersed, and cells processes interconnected.* ***(b)*** *Cultured cortical neurons transfected with ChR2 where the cell expresses high level of GFP.*

To interface neuronal network with an integrated photonic chip, neurons need to express photosensitive proteins. We tried different methods of transfection and we found that the most suitable method is the nucleofection. We then, transfected cells with pAAV-Syn-ChR2(H134R)-GFP, in short ChR2. Since the single channel conductance of ChR2 is very small, high expression levels of the protein are required to fire neurons reliably. For that reason, we optimize condition of transfection in order to obtain high level of expression of Chr2 evaluated by measurement of fluorescent level of the GFP reporter (Fig. 8).

6. Addressable arrays of neuron exciters on chip (Clara Zaccaria, Davide Bazzanella, Mattia Mancinelli)

To optically excite in vitro neuronal cultures via optogenetics, we design photonic integrated circuits, where waveguides will convey light to scattering structures to focus the optical signal on the specified neurons. Since the selected rhodopsin is ChR2, which can be activated by blue light with wavelength of 488 nm, the photonic chip has been designed for this visible range, with Si_3N_4 waveguides embedded in SiO_2 cladding.

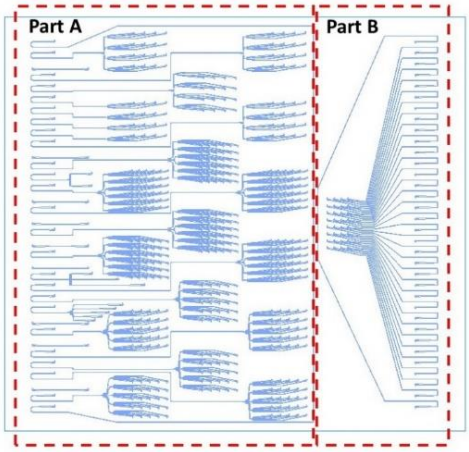

Figure 9. *The chip design*.

As shown in figure 9, the chip is divided into two main areas, each presenting 32 input grating couplers on the chip perimeter. In part A there are three different types of scattering matrices, composed by 4x4, 5x5, and 6x6 grating scatterers. Every input coupler provides light to all the output grating of a matrix, except in one case where each row of the matrix is connected to a different input coupler. Differently, in part B there is only one 4x8 matrix, in which every scatterer is connected to a single input coupler. This section will be important for experiments in which single neurons must be addressed.

The key devices in the array are the grating couplers (Fig. 10) which were designed to create a spot with a diameter of nearly 10 µm on the exact plane where the neurons lay, i.e. at 5 µm from the waveguide plane. The design of the grating was performed using wave-transfer matrix theory. The total field scattered is calculated as the sum of the scattering field of each period of the grating structure, which has been parametrically chosen. In order to obtain the desired scattered light distribution and spot size, the geometry of the grating has been generated using optimization algorithms. The target scattering distribution has a Gaussian profile (Fig. 10, bottom). In Fig. 11 the results of the simulation of one optimized grating scatterer are shown.

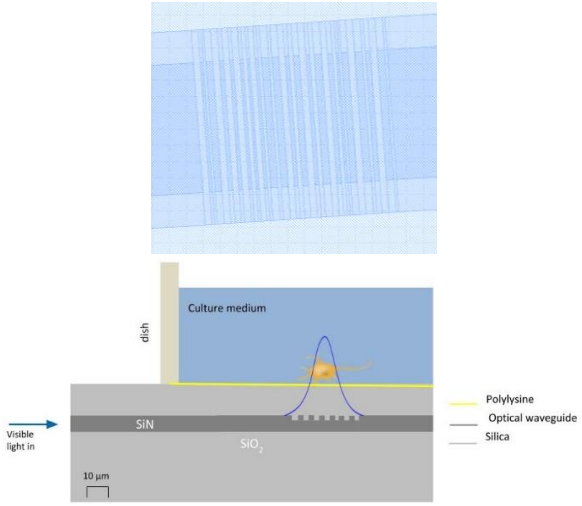

Figure 10. ***(top)*** *the designed grating scatterer.* ***(bottom)*** *a sketch of the cross section of the system.*

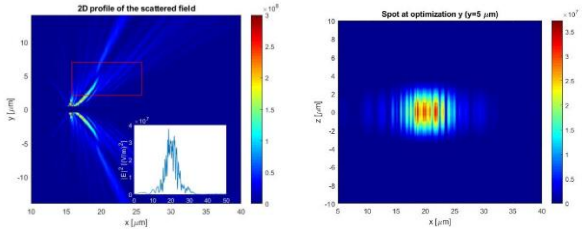

Figure 11. (a) *2D profile distribution of the light scattered by the grating.* ***(b)*** *spot created on the surface of the chip.*

7. Neuromorphic photonics in silicon photonics (D. Bazzanella, P. Bettotti, M. Mancinelli, E. Sangineto)

A first chip was fabricated within a MPW scheme, Fig. 12, to implement a neuromorphic photonic neural network. We designed two different networks. The first exploits the same mechanisms of deep learning, although with some additional physical requirements. We have an all-optical feed-forward network and a complex valued perceptron. The second is based on the paradigm of reservoir computing, such as a swirl network and SCISSOR (side-coupled integrated spaced sequences of optical resonators) based reservoir networks.

We are currently working on developing numerical code that simulates the physical response of a defined silicon structure to a generic input signal. At this time, we are concentrating on the response of the microring resonator structure, either alone or coupled together in the SCISSOR configuration. In principle, one has to take into account all the important nonlinear phenomena in silicon, such as the Kerr effect, the two-photon absorption (TPA), the Free Carrier Dispersion (FCD), the Free Carrier Absorption (FCA), and the Thermo-optical effect. This problem is usually resolved with 'brute-force' using ordinary differential equation (ODE) solvers with coupled equations. This method is, however, quite computing intensive. We are pursuing the reduction of the computational intensity in order to expand the simulation to include the specific topology of the connection between simple structures.

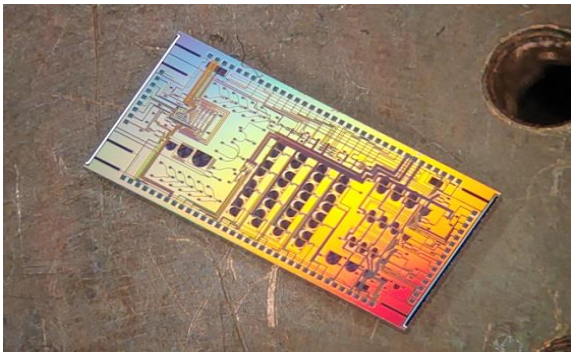

Figure 12. *The fabricated neuromorphic chip. The edge is 5mm long.*

An example of the results obtained by these simulations is shown in Fig. 13, where a structure is fed with a time dependent input signal (solid blue line) and must activate its output (solid red line) only when a specific pattern is recognised. The output of the structure is appreciably close to the target response (dashed black line).

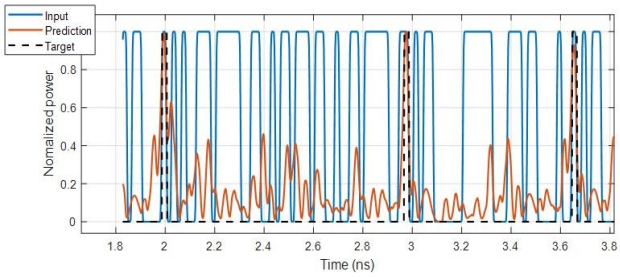

Figure 13. *Example of timeseries obtained with the simulations. Feeding the input signal (solid blue line) to the structure produces a specific output signal (solid red line), which should be compared to the target response (dashed black line).*

Each architecture can fruitfully perform a finite set of tasks for which it is designed and our devices are no exception. Moreover, in order to compare the results we obtain for different structures and training implementation among them and to results of other research groups, we ought to define some benchmarks. For this reason, we identified a list of problems on which we can test our devices: XOR problem, pattern recognition (MNIST), bit-string discrimination, and FEC in long-haul optical links. In this way we can test the structure, compare their performance, and define the best field of applications suitable for the device under test.

8. Optical time delay reservoir computing using silicon microring resonators (Giovanni Donati)

Reservoir computing (RC) has been introduced as a new approach to the general concept of recurrent neural networks, aiming to simplify the network structure and the training process adopting the following configuration: one input layer, an ensemble of nonlinear nodes randomly connected with a fixed strength called reservoir, and a trainable linear output layer. Quite interestingly, it is possible to use the complex dynamic of only one nonlinear node subjected to a delay feedback to produce a 'virtual' reservoir (Fig. 14).

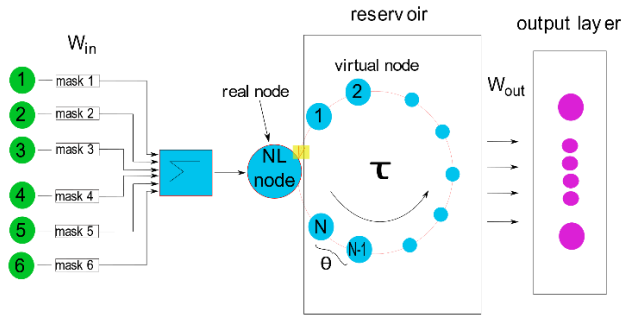

Figure 14. *General delay RC scheme with many input channels (often only one channel is used): after pre-processing the input with a specific mask for each channel (playing the role of the input weights) the signals are summed and, then, used as input to the nonlinear node. The response of this last is then acquired and, at specific different times, they provide the state of the correspondent virtual nodes. These values are then used to evaluate the output layer state. Moreover, virtual node line is reinjected through a feedback to the nonlinear node.*

The possibility to process information exploiting only one nonlinear node and the consequent simplification from a hardware implementation point of view, drives this research which aims to transfer this approach in integrated silicon photonics, using as a real node structure based on silicon microring resonators, where the time-delayed feedback is simulated by connecting the through port to the add port, or by connecting the output port to the input one, as in Fig. 15.

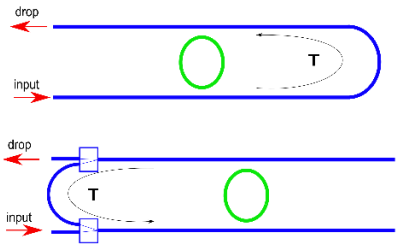

Figure 15. *Add-drop microring resonator subjected to delay feedback in two possible configurations.*

The computational properties of such systems, as the consistency and the memory capacity will be estimated, as well as the capability of this fundamental computational unit to solve certain tasks. At next step, the strategy to follow will be to upgrade the system adding progressively more microring resonators and studying the additional complex dynamics and how these modify the computational properties. SCISSOR and Vernier configurations are possible future candidate topologies to be investigated. Of interest is the possibility to make the system sensible to past input information with different weights: one provided by the feedback line (τ), and the other inherent the geometry of the nonlinear node under study.
This work is carried out within a joint co-tutelle agreement with the University of the Balearic Islands (Spain).

9. An Extreme Learning Machine with silicon photonics (Dhouha Jemmeli)

The main task of machine learning (ML) is to infer a reasonable model to describe the observed data and use the inferred model to make predictions. ML is particularly useful for optimization and performance prediction of systems that exhibit complex behaviors, analytical models are difficult to derive, and numerical processes take longer time. In this case, photonics became a new way for low power, efficient and fast ML implementations. A single hidden layer feedforward neural network with randomly generated hidden nodes and analytically computed output weights is called an extreme learning machine (ELM). When ELM is implemented in a photonic platform, we call it PELM.

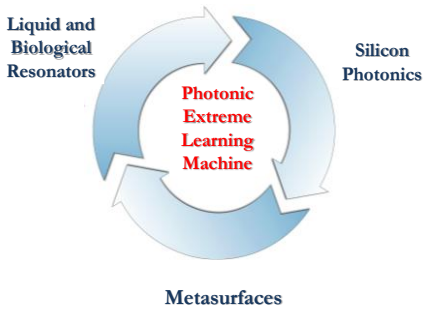

Figure 16. *Different hardware platforms implement the same machine learning architecture*

In the PELM project, different platforms will be demonstrated (Fig. 16) which are described by a unique computational algorithm implemented by different physical realizations of the computation nodes. The various platforms will have also different output weights training. This training will be realized by thermal tuning of the micro-ring resonances in the silicon photonic PELM. On the contrary, it will be achieved via the controlled spatial light modulation of the multimode light scattered by the metasurfaces or by the whispering gallery mode in spherical droplet resonators in the other PELM. Modelling, design and on-demand

fabrication will allow applying the PELM concept to these different and complementary technologies where proof-of-concept applications will be demonstrated, ranging from computing and optical function synthesis, to strain gauge sensor and cancer detection or monitoring.

10. Time response of a waveguide/microresonator system (Stefano Biasi, Pierre Guillemé, Giorgio Fontana)

The figure of merit of a microresonator coupled to a bus waveguide device is the quality factor Q, which quantifies its light storage capacity. During the years, several experimental techniques have been developed to estimate Q, from the simple measurement of the full width at half maximum of the resonance to the more complex cavity ring down spectroscopy. The first method uses the definition of Q as the ratio of the resonance frequency and its width, while the second considers the energy stored in the resonator. Although the spectral measurement of a Lorentzian lineshape is easy, the progress in the fabrication yields high-Q resonators that require a very high spectral resolution. In addition, this simple measure does not provide direct information on the coupling regime. Specifically, a bus waveguide can be coupled to a microresonator in one of the three characteristic regimes: over-coupled, critical-coupled and under-coupled. These regimes are defined by the interference between the light propagating in the bus waveguide and that circulating in the microresonator. Depending on the coupling regime, this interference changes determining both the intensity and the phase delay of the output signal. The knowledge of the time dependent electric field permits, through its particular evolution, to understand the coupling regime of a waveguide/microresonator system. Exploiting the Green function, we propose an analytical complex expression for a single Lorentzian transmission response. It is obtained by exciting the bus waveguide through a rectangular pulse and it allows extracting the intrinsic and the extrinsic damping rate. Moreover, finite difference time domain (FDTD) simulations illustrate the analytical solution and permit to understand the meaning of the different coupling regimes.
Fig. 17 shows the output electric field as a function of time for a resonant rectangular pulsed excitation of a microresonator. Precisely, panels (a), (b) and (c) display the over-, critical- and under-coupling regime. The inset shows the electric field distribution at the different times indicated by the red pins in the temporal evolution. While the red lines refer to the analytical solution. The three distinct temporal evolutions allow distinguishing between the different coupling regimes. Indeed, in the over-coupling case, the interference between the field propagating in the bus waveguide and the one exiting from the ring completely destroys the exiting wave. Thus, the stationary regime is reached after more round-trips at time 4 where the wave exiting from the resonator prevails.

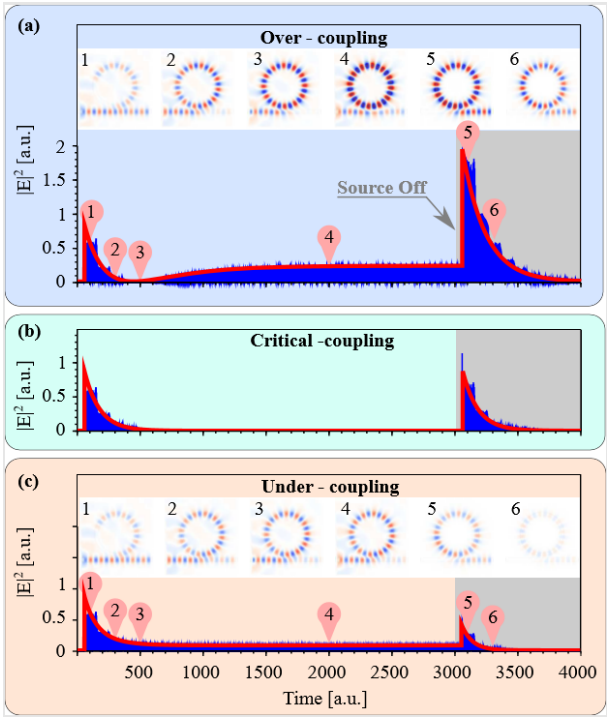

Figure 17. *FDTD simulations of a waveguide/microresonator system excited trough a resonant CW source of duration 3000 a.u. The inset imagines show the electric field distribution at the different times indicated by the red pins. The red lines display the fit with the analytical model.*

On the contrary, in the under coupling regime the trip losses become equal to the coupled power before the power inside the microresonator becomes large enough to observe the destroy interferences. In fact, the stationary regime is reached without destroying the output field (see time 4 of fig. 17). While in the critical coupling, the stationary regime corresponds to the scenario where the interferences exactly destroy the exiting wave. All panels show an exponential behavior when the source is turn on and turn off. This is directly connected to the charge and discharge of the system and therefore to the quality factor.

11. Towards the nonreciprocal response for forward and backward propagation (Stefano Biasi, Riccardo Franchi, Alberto Munoz De Lasheras)

One of the limiting factors of microresonators with high/ultra-high quality factor is the backscattering of propagating modes. This gives rise to a wave that propagates in the opposite direction with respect to the input one. The stochastic nature of the surface roughness, which is responsible for the backscattering, leads to a simple statistical approach, that results in a symmetrical resonance splitting in the transmission. This can be treated by a Hermitian coupling directly linked to a conservative exchange of energy between the counterclockwise (CCW) and clockwise (CW) modes. In this scenario, the Hermitian coupling and the Lorentz's theorem enforce to have the same reflection in

both directions of excitation. In the case of multi-modal microresonators, the transmission may exhibit asymmetric resonance doublets (i.e. different peak depths). This can be explained by considering dissipative coupling coefficients. In non-Hermitian systems, whereas the Lorentz reciprocity enforces equal transmission in both directions, the reflection can be completely different. This can lead to a scenario where there is a maximum contrast between the amplitudes of reflections in the two directions. Formally, this occurs when the conditions of exceptional points are met (when the eigenvalues and their eigenvectors simultaneously coalesce and become degenerate). Here, there is no longer a doublet and the amplitude of the reflection is maximum in one direction and is reduced to zero in the other. Therefore, exploiting these non-Hermitian coupling coefficients one can create unidirectional mirrors. Since these parameters are connected to the surface roughness and to the multimodal nature of the resonator, the control of the behavior of a simple microresonator coupled to a bus waveguide is difficult. However, it is possible to introduce new geometries capable of forcing the exchange of energy from CW to CCW or vice versa. This has been recently demonstrated by embedding an S shape waveguide inside a microring resonator. We call these systems a taiji microresonator (see inset of Fig. 18). Since the thermo-optic and the Kerr coefficient depend on the field intensity inside the cavity the different distributions of energy among the counter-propagating mode break the Lorentz reciprocity theorem and, therefore, induce different transmission for forward and backward propagation.

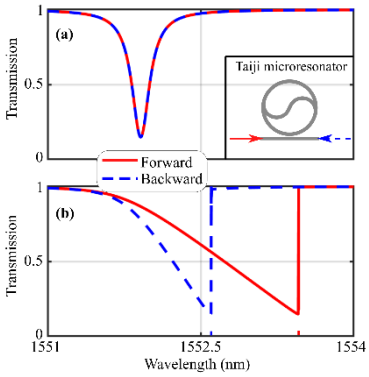

Figure 18. *Numerical transmission of a taiji microresonator as a function of the incident wavelength. The inset of figure (a) represents a sketch of the taiji microresonator. The solid red (dashed blue) lines highlight the forward (backward) propagating mode. Panel (a) shows the low-power regime while panel (b) displays the high-power response. The spectra are obtained scanning the wavelength from blue to red.*

Fig. 18 shows the numerical simulation of the transmission for a taiji microresonator as a function of the incident wavelength. Fig. 18 shows the linear (low-power, 18a) and nonlinear (high-power, 18b) response, respectively. The low-power response exhibits the typical symmetric Lorentzian where the transmission is the same in both excitation directions. Indeed, the red and blue lines overlap. In this scenario, the total losses are the same for the two propagation directions but they are distributed in a different way between reflection and absorption. Indeed, for the forward (backward) propagation, the reflection assumes the maximum (minimum) value. On the other hand, at high-power, the Kerr nonlinearity gives rise to a typical triangular shape in the transmission spectra (see Fig. 18b). Interestingly, the different distributions of the energy inside the cavity cause a distinct wavelength position of the resonance jump and, therefore, a nonreciprocal transmission response. Indeed, in the forward propagation, the coupling with the S-branch induces a counter-propagating mode, which gives rise to an increase of the energy inside the cavity. On the contrary, in the backward propagation, this amount of energy is lost at the ends of the S-branch.

12. Electric field induced second harmonic generation in silicon waveguides using two different poling structures made by lateral p-n junctions (Riccardo Franchi, Claudio Castellan)

Second harmonic generation is not allowed in silicon because of its centrosymmetry which implies a zero second order susceptibility ($\chi^{(2)}$). Recently, this has been overcome by using a constant electric field coupled to the silicon third order nonlinearity ($\chi^{(3)}$) and inducing the so called Electric Field Induced Second Harmonic Generation (EFISHG). To have a constant electric field across a silicon waveguide, lateral p-n junctions are fabricated, Fig. 19a.

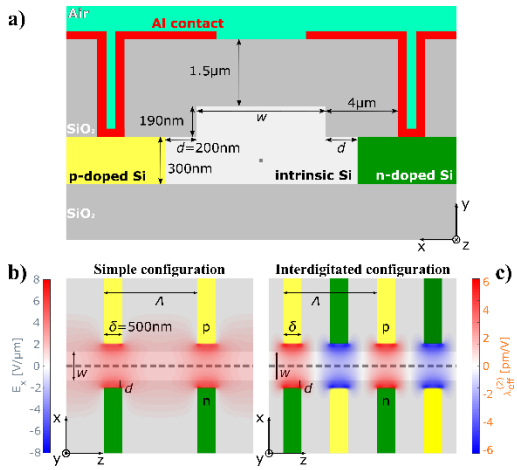

Figure 19. ***(a)*** *Waveguide cross section.* ***(b), (c)*** *Top views of the two configurations, simple and interdigitated with the simulated electric field and* $\chi^{(2)}_{eff} = 3E_{d.c.}\,\chi^{(3)}$ *with the reverse bias voltage of 3.5V.*

In order to obtain EFISHG, it is also necessary to satisfy the phase-matching condition: $n_{eff,SH} - n_{eff,p} = 0$, where

$n_{eff,SH}$ and $n_{eff,p}$ are the effective mode indices of the SH and pump wave. This is achieved by using the poling technique where a periodical modulation Λ of $\chi^{(2)}_{eff}$ is used. The quasi phase-matching condition (QPMc) reads $n_{eff,SH} - n_{eff,p} = \frac{\lambda_{SH}}{\Lambda}$, where λ_{SH} is the SH wavelength. In QPMc, the efficiency of EFISHG is linked to the variation of $\chi^{(2)}_{eff}$ along the wave propagation direction. We designed and measured two different poling geometries: simple and interdigitated, Fig. 18b and 18c. Since in the interdigitated configuration, unlike in the simple one, the electric field across the waveguide changes sign along the propagation direction, a higher generation efficiency with the same applied voltage is expected for the interdigitated than for the simple configuration.

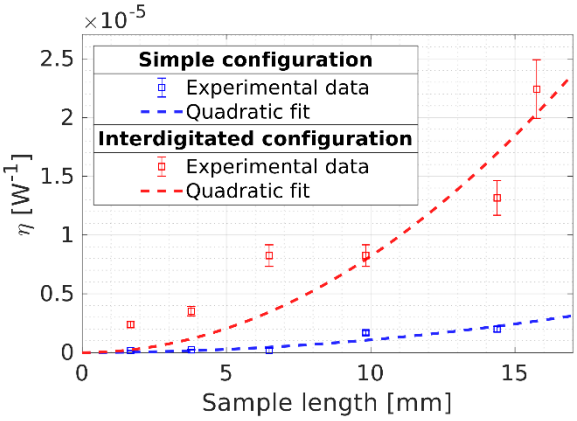

Figure 19. *SHG efficiency, η, as a function of the sample length, for the simple and interdigitated configurations.*

Fig. 19 reports the measured conversion efficiency η as a function of the sample length. As expected, η is about ten times higher for the *interdigitated* case than for the simple. Furthermore, the effective second order susceptibility obtained at 3.5V for the two configurations is $\Delta\chi^{(2)}_{eff,S} \simeq$ 0.14pm/V for the *simple* configuration and $\Delta\chi^{(2)}_{eff,I} \simeq$ 0.64pm/V for the *interdigitated* ones.

13. Modeling second harmonic generation by lateral pn junction (Chiara Vecchi)

Lateral *pn* junctions across periodically poled silicon waveguide induce an effective $\chi^{(2)}$ due to the induced DC electric field. Measurements of the second harmonic generation (SHG) efficiency in these waveguides show a multiple peaked spectrum which suggests disorder in the waveguide parameters. Two kinds of disorder can be present: disorder in the geometry of the waveguide and disorder in the poling period. Since the generated power P_{SH} in SHG can be written as $P_{SH} = P_p^2 \left|\tilde{\gamma}^{(2)}_{SH}\right|^2 L^2 S$ with S defined as $S = \frac{1}{L^2}\left|\int_0^L s(z)e^{i\Delta\beta z}\right|^2$ and L the waveguide length, P_{SH} is directly proportional to the S function. S shows a dependence on $\Delta\beta$, which is the mismatch function between the SH and pump effective indexes, and on $s(z)$, which is the poling function. We, therefore, modelled the SHG by introducing a disorder in the waveguide geometry (gaussian distribution of the width w of the waveguide centered around the nominal value with a variance σ_w) and in the poling period (random function with a gaussian distribution around the nominal value Λ with a variance σ_Λ). Fig. 20 shows the simulation results. Increasing the disorder in the waveguide geometry, S broadens and weakens, but is single-peaked. However, increasing the disorder in the poling period induces a multiple-peaked S function, while the value of S is barely affected. Combining the two kinds of disorder is possible to model the experimental results.

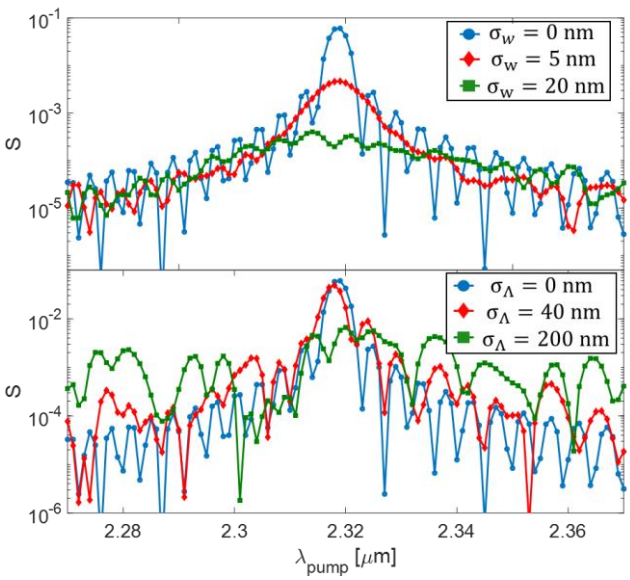

Figure 20. *Results of the simulations of the S function. Different lines refer to different standard deviations in the disorder. (top) Effects of the disorder on the waveguide geometry. (bottom) Effects of the disorder on the poling period.*

14. Estimation of the nonlinear coefficients for a LPCVD SiN waveguide through stimulated FWM (Riccardo Franchi, Stefano Signorini)

Silicon nitride is a viable platform to develop nonlinear and quantum technologies thanks to the wideband transparency and the relatively high nonlinearity. An important issue in using stoichiometric Low Pressure Chemical Vapor Deposition (LPCVD) silicon nitride is the high stress that is generated due to the thermal expansion mismatch with the silicon buffer. This issue can be mitigated by developing materials with slightly different stoichiometric composition. Here, we study the nonlinear coefficient of a LPCVD silicon nitride material that achieves a low stress thanks to a silicon excess with respect to the stoichiometric value.
To estimate the third order nonlinear coefficients, we used

the stimulated Four Wave Mixing (sFWM). The sFWM is a third order nonlinear phenomenon that converts two pump photons, having the same wavelength, into two other photons, signal and idler, having different wavelengths; moreover, to increase the rate of this process, it is stimulated by adding an input beam having the wavelength of the *signal*.

To achieve this process it is necessary to satisfy two relations: the energy conservation, $2\hbar\omega_p = \hbar\omega_s + \hbar\omega_i$, and the phase matching, $2k_p = k_s + k_i$. If the two conditions are satisfied, the following relations are obtained: $P_i = 4|\gamma^{(3)}|^2 P_p^2 P_s L^2 \left(sinc\left(\frac{\Delta\beta\, L}{2\pi}\right)\right)^2$, $\gamma^{(3)} \approx \sqrt{\frac{P_i}{4P_p^2 P_s L^2}}$, $n_2 = \gamma^{(3)} A_{eff} \frac{\lambda_p}{2\pi}$ and $\chi^{(3)} = \frac{4}{3} n_2 \varepsilon_0 n^2 c$. In our case the *pump* wavelength is fixed at 1.55µm. Using a Single Photon Avalanche Photodiode (SPAD) coupled to a monochromator, we measured the spectrum at the output of the waveguide without (spontaneous FWM) and with the stimulating seed, see Fig. 21.

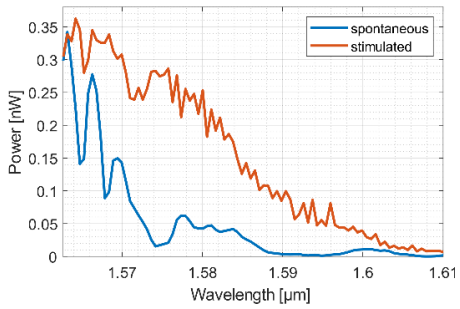

Figure 21. *Output spectrum for the Spontaneous and stimulated FWM. In the stimulated measurement, the seed wavelength is changed in order to measure the stimulated spectrum over a broad spectral band.*

From these measurements we estimate the third order nonlinear coefficients: $\gamma^{(3)} \simeq 0.3W^{-1}m^{-1}$, $n_2 \simeq 7.5 \times 10^{-20} m^2/W$ and $\chi^{(3)} \simeq 9.5 \times 10^{-22} m^2/V^2$.

Comparing the obtained n_2 with the literature, see Tab. 1, it can be observed that the value obtained in other works with a technology similar to ours is about 1.5 times higher than the one we obtained. This is probably due to the different material quality and the waveguide geometry. We can also observe that silicon has a third order nonlinearity almost two orders of magnitude higher than LPCVD SiN, but silicon itself does not have a second order nonlinearity and absorbs light with wavelengths lower than 1.1 µm. SiN, on the other hand, has a second order nonlinearity and has much smaller losses around 775nm.

	$n_2\ [m^2/W]$
SiN LPCVD LS77	7.5×10^{-20}
SiN LPCVD	1.1×10^{-19}
SiN PECVD	6.94×10^{-19}
c-Si	$4.3 - 6 \times 10^{-18}$

Table 1 *Comparison between n_2 in units of m^2/W for different materials.*

15. Heralding mid infrared single photons on a silicon chip (Stefano Signorini, Sara Piccione)

Quantum photonics promises to revolutionize the technologies based on its classical counterpart, with improved performance and new applications on the integrated platform. In particular, the quantum properties of light can significantly boost optical sensors. By exploiting entanglement or quantum based protocols, sensitivity and resolution of optical sensors can be highly increased. This is particularly appealing for the mid infrared (MIR) spectral range, where absorption spectroscopy is used to probe the concentration of molecules in a volatile sample. To implement an on-chip MIR quantum gas sensor, an integrated source of MIR single photons is required.

In this work, we demonstrate the generation of heralded single photons beyond 2 µm via intermodal four wave mixing (FWM) in a silicon rib waveguide. We pump, at 1550 nm, the fundamental and first transverse electric (TE) spatial modes in a multimode waveguide to generate two correlated photons: one at 1260 nm on the TE0 and one at 2013 nm on the TE1. The higher energy photon (idler) is measured to herald the lower energy photon (signal), which exhibits a single photon behaviour. To manage the different propagation modes for the signal and pump waves, we designed a chip with asymmetric directional couplers (ADCs), as shown in Fig. 22.

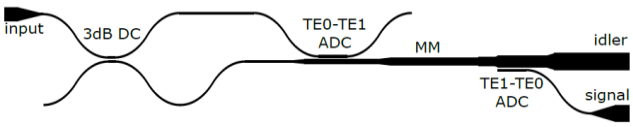

Figure 22. *Chip used for intermodal FWM in a multimode waveguide (MM). The input 3dB directional coupler (DC) splits the pump. The ADCs are used to in/out-couple the TE1 mode.*

The performance of the source is highly affected by the detection efficiency of the signal photon. Since no single photon detectors are available in the MIR, an upconversion system is used. The MIR photons are spectrally shifted to the visible before being detected. This process limits the overall efficiency of the system, but still maintains a coincidence-to-accidental ratio (CAR), Fig. 23a, sufficiently high to perform quantum measurements (max CAR ≈ 53(5)). We also characterized the spectral purity of the MIR photon by measuring its second order correlation function $g^{(2)}$ in a Hanbury-Brown and Twiss interferometer, Fig. 23b. We measured a maximum purity of 0.45(3). With a broader pump bandwidth, we expect to achieve much higher purities without the use of output filters, thanks to the discrete

band phase matching of intermodal FWM, thus keeping high heralding efficiencies. In order to assess the single photon character of the heralded signal photon, we measured the signal $g^{(2)}$ conditioned to the detection of the idler, Fig. 23c. We measured an anti-bunching dip of 0.11(4), demonstrating that our heralded source actually operates in the single photon regime.

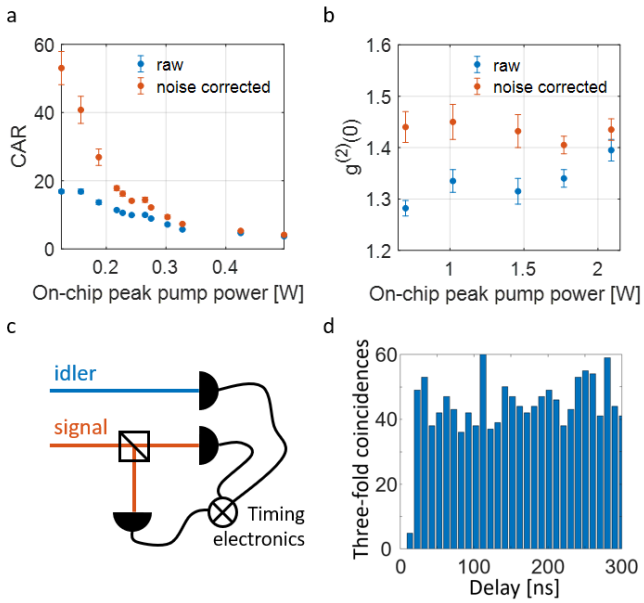

Figure 23. ***(a)*** *CAR and* **(b)** *$g^{(2)}(0)$ as a function of the on-chip peak pump power.* ***(c)*** *Setup for conditioned second order correlation function.* ***(d)*** *Anti-bunching measurement with the setup in c).*

16. Spin-momentum single particle entanglement of laser photons (Nicolò Leone, Stefano Azzini)

Single-Particle Entanglement (SPE) is a peculiar type of entanglement in which two degrees of freedom (DoFs) of a photon are entangled. Compared to inter-particle entanglement, SPE requires only linear optical components as beam splitters and polarization rotators and no high power sources are involved, like in Spontaneous Parametric Down Conversion and Four Wave Mixing processes. In our experiment, we have generated SPE state using as DoFs the momentum, i.e the direction of propagation, and the polarization of the single photon. Photons are generated by an attenuated laser beam. The entire setup can be divided into three stages: the generation stage, in which the entanglement is actually created; the preparation stage, in which the state is manipulated, i.e. the qubits corresponding to the two DoFs are rotated using linear optical components; the detection stage, where four Single Photon Avalanche Detectors (SPADs) are used to measure the single-photon entangled states.

To verify the entanglement, a Bell test is performed looking for a violation of the Clauser, Horne, Shimony and Holt (CHSH) inequality expressed by the correlation function S:

$$|S(\phi,\phi',\theta,\theta')| < 2$$

S is composed by the different detection events, obtained for each experimental realization, where ϕ and θ are, respectively, the different rotations of momentum and polarization. Note that, for obtaining a single value of S, four measurements are necessary: (ϕ,θ), (ϕ',θ), (ϕ,θ') and (ϕ',θ'). The experimental data and the theory are reported in Fig. 24. We measured a maximum violation of $S = 2.60 \pm 0.08 > 2$. The photon DOFs are indeed entangled.

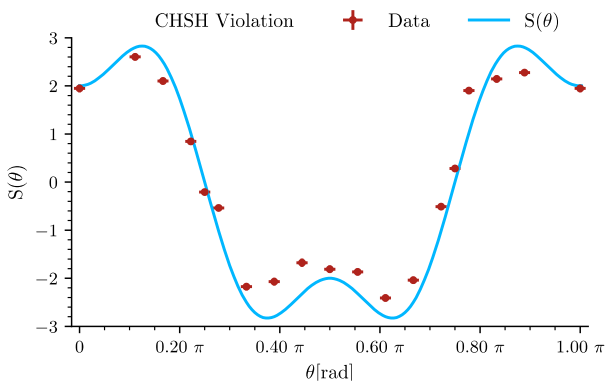

Figure 24. *S correlation function versus the angle θ that controls the polarization DoF. The red points are the experimental data, while the blue solid curve represents the theoretical behaviour.*

The violation of the SCHSH inequality rules out the possibility of having a Non-Contextual Hidden Variables description. Since we have used an attenuated laser, we proved also that SPE can be obtained with no need of a pure single-photon source. This enables cheap and low power sources in quantum photonics applications, in contrast to what happens for inter-particle entanglement where high power lasers are needed. Moreover, if we increase the power of the attenuated laser, multi-photon states are generated. To handle these, we must refer to the effective behaviour of the operators involved in the experiment. We can divide them into two categories: the operator that generates the entanglement and performs qubits rotations, and the projection operators in the detection stage used to build the Bell test. Regarding the first category, their cumulative action in the case of multi particle states is directly obtained by the action of the operator at the single particle level, since all the optical elements are linear. Regarding the second category, it can be proved that each of the projectors commutes with the number of particles operators, i.e. the detection stage cannot distinguish between a multi particle state and a single particle one. These final considerations prove that SPE is a type of entanglement which is insensible to the number of particles, i.e. which can be created using not only pure single photon sources but also using multi photon ones, like common lasers.

17. Self-Testing Quantum Random Numbers Generation (QRNG) on a silicon photonic chip (Nicolò Leone, Stefano Azzini)

A fundamental task in random numbers generation is to guarantee the security of the generated sequence. This can be done by estimating the minimum entropy H_{min}, a parameter that represents the amount of intrinsic randomness present in the sequence itself. It feeds also randomness extractors to generate a nearly perfectly random sequence. In this scenario, the Semi-Device Independent protocols have pushed the security limits even further, since the estimation of H_{min} is performed treating a part of the system as a black box, e.g. without making any assumption about it. Here we applied the Semi-device independent methodology to our integrated QRNG (quantum random number generator). In our QRNG, an integrated emitter, which is a mini silicon photomultiplier (SiPM), and a detector, that is an integrated-passively-quenched SPAD, are both integrated on the same chip. Depending on a pseudo random bit x, the emitter is biased to emit a bunch of photons (x=1) or to stay inactive (x=0). For each bit x, the SPAD perform a measurement giving as output a bit y, where y is y=1 if a detection occurred and y=0 in the other cases. Note that the sequence of y is also the raw sequence of random numbers. Since the emitted state has a non-zero component of the vacuum, the two states corresponding to the emission and no-emission are not orthogonal. This implies that the SPAD is in the uncertainty condition of detecting no photons even if they are present. This makes quantum the generation process of the random numbers sequence. A key parameter for the mean H_{min} estimation is the overlap between the two states emitted for x=0 and x=1, which is connected to the mean number of photons emitted in a given time interval. In order to characterize it, an estimation of the number of photons emitted by the integrated emitter is performed. By building the conditional probability P(y|x) and knowing the value of the overlap between the vacuum and the emitted state, it is possible to obtain a lower bound to the generated H_{min}.

Fig. 25 shows H_{min} as a function of the mean number of photons n_γ and k, a parameter that takes into account possible assumption to better estimate the flux of photons that is effectively seen by the integrated detector. If Φ_v is the vertically emitted photon flux from the emitter and Φ_h the horizontally emitted photon flux that is measured by the detector, we write $\Phi_v = k\,\Phi_h$. Then k=2 means that, due to geometry, the horizontal photon flux is half of the vertical one. If k=1, the two are equals. However, the evaluation of the exact value of k is not easy due to complexity of the entire structure. In this case a good choice is to assume k=1, this allows giving a lower H_{min} bound that takes into account the difficulty in the estimation of k, i.e. reducing the possible weakness of the protocol. We found a maximum H_{min}=0,6% for k=1, meaning that we can extract 6 certified random numbers out of 1000 generated numbers.

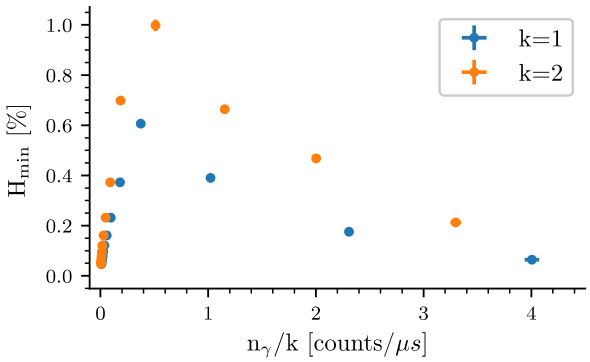

Figure 25. *Minimum entropy H_{min} as a function of the mean number of emitted photons n_γ/k. The blue dots are the values for k=1, while the orange dots refer to k=2. Note that H_{min} increases as k increases, since the overlap between the emitted state and the vacuum state is larger for higher k.*

For more info:

Nanoscience Laboratory
Department of Physics
University of Trento
via Sommarive 14
38123 Povo- Trento (Italy)
http://nanolab.physics.unitn.it/

Laboratory assistant
Dr. Chiara Rindone
email chiara.rindone@unitn.it
phone +39 0461 283172